

**Magnetization tunable Weyl states in EuB<sub>6</sub>**Jian Yuan,<sup>1,\*</sup> Xianbiao Shi,<sup>2,\*</sup> Hao Su,<sup>1</sup> Xin Zhang,<sup>1</sup> Xia Wang,<sup>1,3</sup> Na Yu,<sup>1,3</sup> Zhiqiang Zou,<sup>1,3</sup> Weiwei Zhao,<sup>2</sup>  
Jianpeng Liu,<sup>1,4,†</sup> and Yanfeng Guo<sup>1,4,‡</sup><sup>1</sup>*School of Physical Science and Technology, ShanghaiTech University, Shanghai 201210, China*<sup>2</sup>*State Key Laboratory of Advanced Welding and Joining, and Flexible Printed Electronic Technology Center, Harbin Institute of Technology, Shenzhen 518055, China*<sup>3</sup>*Analytical Instrumentation Center, School of Physical Science and Technology, ShanghaiTech University, Shanghai 201210, China*<sup>4</sup>*ShanghaiTech Laboratory for Topological Physics, ShanghaiTech University, Shanghai 201210, China*

(Received 14 October 2021; revised 28 July 2022; accepted 29 July 2022; published 9 August 2022)

The interplay between magnetism and topological band structure offers extraordinary opportunities to realize rich exotic magnetic topological phases such as axion insulators, Weyl semimetals, and quantum anomalous Hall insulators, and therefore has attracted fast growing research interest. The rare-earth hexaboride EuB<sub>6</sub> represents an interesting magnetic topological phase with tunable magnetizations along different crystallographic directions, while the correlation with the topological properties remains scarcely explored. In this work, combining magnetotransport measurements and first principles calculations, we demonstrate that EuB<sub>6</sub> exhibits versatile magnetic topological phases along different crystallographic directions, which tightly correlate with the varied magnetizations. Moreover, by virtue of the weak magnetocrystalline anisotropy and the relatively strong coupling between the local magnetization and the conduction electrons, we show that the magnetic ground state of the system can be directly probed by the anisotropy in the magnetotransport properties. Our work thus introduces an excellent platform to study the rich topological phases that are tunable by magnetic orders.

DOI: [10.1103/PhysRevB.106.054411](https://doi.org/10.1103/PhysRevB.106.054411)**I. INTRODUCTION**

The correlation between magnetism and nontrivial topological electronic band structure is currently one of the central topics in the field of topological phases of matter. To achieve crucial insights into this issue, topological phases with strong spin-orbit coupling (SOC), low structural symmetry, and long-range magnetic order could serve as an excellent platform [1]. In such systems, the spin rotation can significantly vary the electronic band structure by the energy of even one order of magnitude larger than the traditional spin Zeeman splitting, thus allowing for more convenient investigation of the tight link between different magnetic structures and the accordingly varied topological electronic states. The van der Waals antiferromagnetic (AFM) topological insulator (TI) MnBi<sub>2</sub>Te<sub>4</sub> is one such clear cut example [2–12], on which the application of an external magnetic field along specific crystallographic directions can drive the magnetic moments to be fully polarized, leading to a topological phase transition from an AFM TI to a ferromagnetic (FM) Weyl semimetal (WSM). Furthermore, the tilting of the Weyl cone could even be controllable in the momentum space via rotating the magnetic field and hence the magnetization direction [5]. In a kagome magnetic WSM, such as Fe<sub>3</sub>Sn<sub>2</sub> and Mn<sub>3</sub>Sn, rotating the magnetization directions by external magnetic field could produce varied pairs of

Weyl nodes through altering the crystal symmetries [13–15]. These magnetic topological materials offer a platform for the study of correlation between magnetism and topological electronic states, as well as more opportunities for the discovery of intriguing topological properties that could be used in next-generation spintronics. However, such magnetic topological phases are still very rare and the exploration is still extremely desirable.

Recently, several rare-earth hexaboride compounds including the Kondo insulators SmB<sub>6</sub> and YbB<sub>6</sub> have been carefully studied focusing on their electronic band structure topologies. The immense studies show that SmB<sub>6</sub> likely has a nontrivial topological nature while YbB<sub>6</sub> seems topologically trivial [16–22]. Meanwhile, another family member of the rare-earth hexaborides, a well-known soft magnetic material EuB<sub>6</sub>, has also been extensively studied due to the novel magnetotransport properties around magnetic phase transition, such as the metal-insulator transition [23,24], the giant blueshift of the unscreened plasma frequency [25,26], the large zero-bias anomalies [27], and large negative magnetoresistance [23,28]. According to previous reports [29,30], a phase transition from the paramagnetic to the FM phase with the moment of Eu<sup>2+</sup> oriented to [001] direction at ~ 15.3 K was observed. At temperatures below ~ 12.5 K, a new FM phase with moment oriented to the [111] direction takes place. Based on the above-mentioned two magnetic ground states, theoretical calculations revealed that EuB<sub>6</sub> is a topological nodal-line semimetal and a WSM for magnetizations along the [001] and [111] directions, respectively. Very recently, angle-resolved photoemission spectroscopy

\*These authors contributed equally to this work.

†liujp@shanghaitech.edu.cn

‡guoyf@shanghaitech.edu.cn

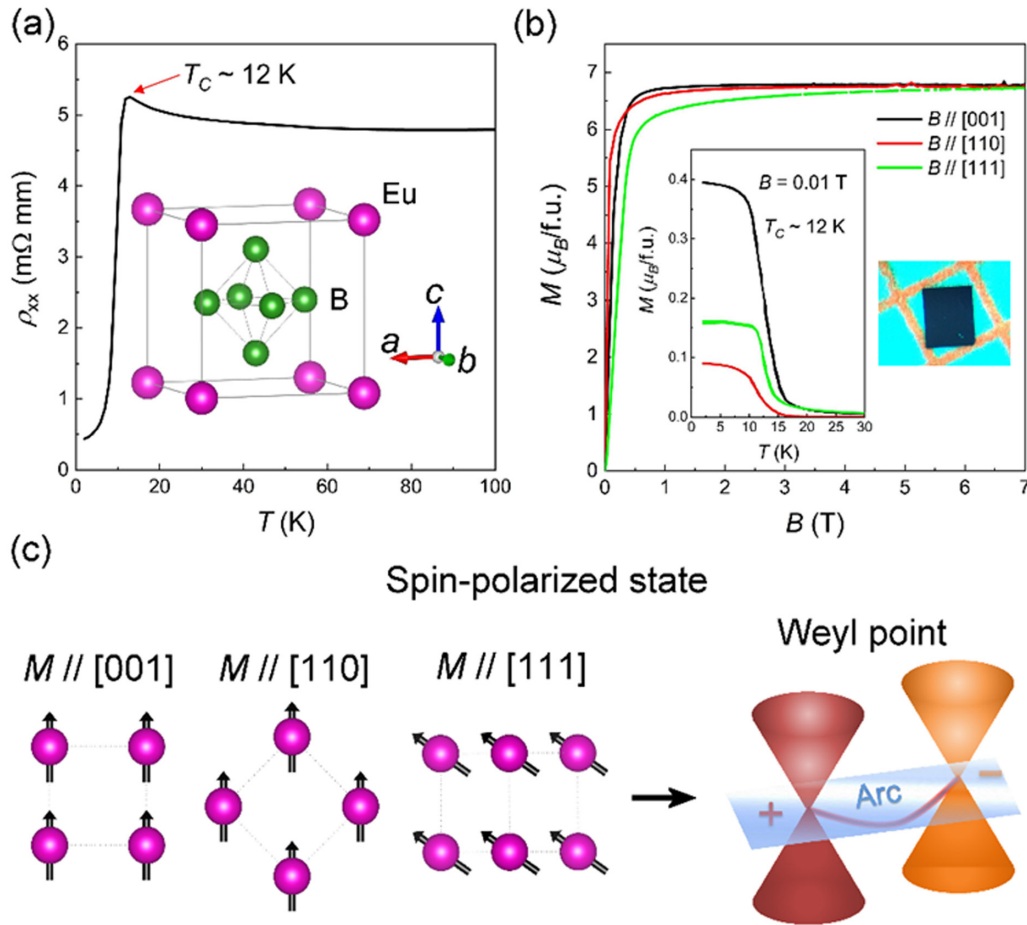


FIG. 1. (a) Temperature dependent longitudinal resistivity  $\rho_{xx}$ . Inset: Schematic crystal structure of  $\text{EuB}_6$ . (b) Isothermal magnetizations measured at 2 K between 0 and 7 T for  $B$  along the [001], [110], and [111] directions, respectively. Inset: Temperature dependent magnetic susceptibility measured at  $B = 0.01$  T and an image of a typical  $\text{EuB}_6$  single crystal. (c) Schematic spin structures for three different spin-polarized states, which could result in the illustrated Weyl state.

measurements presented evidence for the magnetic topological semimetal state in  $\text{EuB}_6$  [31,32]. On the other hand, although the above-mentioned two magnetic phase transitions have been experimentally observed in  $\text{EuB}_6$ , little is known about their specific magnetic structures. Fortunately, the magnetocrystalline anisotropy energy of  $\text{EuB}_6$  is very small such that the orientation of the magnetization ( $M$ ) can be easily modulated by external magnetic field [33,34], which may significantly change the topological electronic structure that can be probed by magnetotransport measurements. This is highly reminiscent of the case of a series of soft AFM materials, such as  $\text{MnBi}_2\text{Te}_4/(\text{Bi}_2\text{Te}_3)_n$  [2–12,35]  $\text{EuCd}_2\text{Sb}/\text{As}_2$  [36,37],  $\text{GdPtBi}$  [38–40],  $\text{MnSb}_2\text{Te}_4/(\text{Sb}_2\text{Te}_3)_n$  [41–49], etc. The soft AFM exchange interactions in these materials can be easily overcome under external magnetic fields that can drive these systems into FM WSMs.

In this work, we demonstrate that  $\text{EuB}_6$  exhibits versatile magnetic topological phases based on magnetotransport measurements and first principles calculations. Moreover, by virtue of the weak magnetocrystalline anisotropy and the relatively strong coupling between the local  $M$  and the conduction electrons, we show that the magnetic ground state of the system can be directly

probed by the anisotropy in the magnetotransport properties.

The  $\text{EuB}_6$  crystals were grown using a method similar to that described in Ref. [50]. Black crystals with shining surface in typical dimensions of  $0.6 \times 0.8 \times 0.2 \text{ mm}^3$  were shown by the picture as an inset of Fig. 1(b). The phase and quality examinations of  $\text{EuB}_6$  were performed on a single crystal x-ray diffractometer equipped with a  $\text{Mo } K\alpha$  radioactive source ( $\lambda = 0.71073 \text{ \AA}$ ). The diffraction pattern presented could be satisfyingly indexed on the basis of a  $\text{CaB}_6$  polytype structure (space group:  $cP7$ , No. 221) with the lattice parameters  $a = b = c = 4.18 \text{ \AA}$ , and  $\alpha = \beta = \gamma = 90^\circ$ . These values are very close to the previously reported ones. The clean reciprocal diffraction patterns without other impurity spots indicate the high quality of our single crystals.

Isothermal magnetizations at various temperatures between 2 and 20 K were measured on a commercial magnetic property measurement system from Quantum Design within the magnetic field range of 0–7 T. Magnetotransport measurements, including the resistivity, magnetoresistance, and Hall resistivity, were carried out in a commercial DynaCool Physical Properties Measurement System from Quantum Design. The resistivity and magnetoresistance were measured in

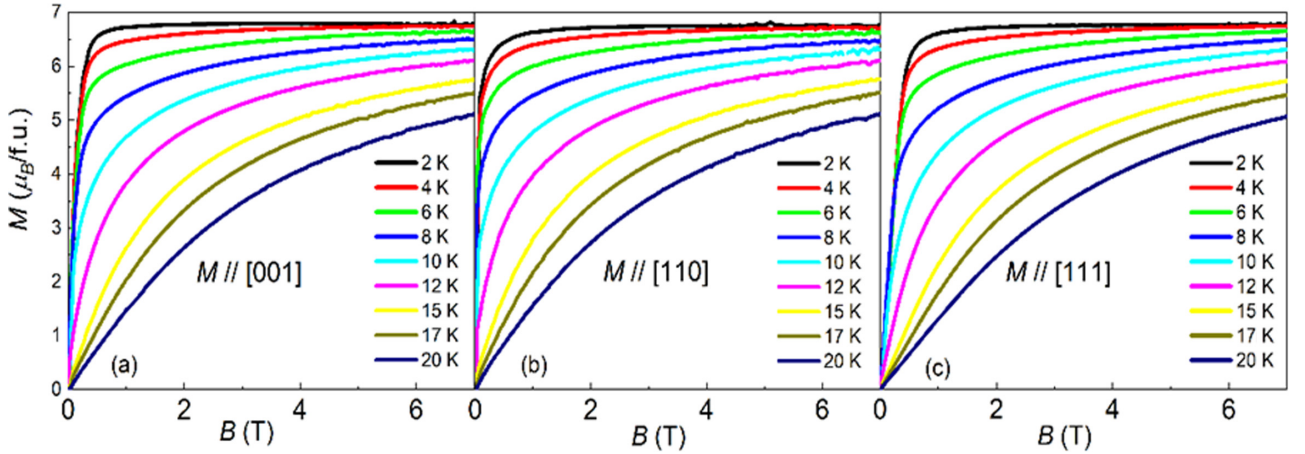


FIG. 2. (a)–(c) Isothermal magnetizations at various temperatures for  $M//[001]$ ,  $M//[110]$ , and  $M//[111]$ , respectively.

a four-probe configuration and the Hall effect measurement was measured using a standard six-probe method.

Present first principles calculations were carried out within the framework of the projector augmented wave (PAW) method [51,52], and employed the generalized gradient approximation (GGA) [53] with the Perdew-Burke-Ernzerhof (PBE) [54] formula, as implemented in the Vienna *abinitio* simulation package (VASP) [55–57]. For all calculations, the cutoff energy for the plane-wave basis was set to 500 eV, the Brillouin zone sampling was done with a  $\Gamma$ -centered Monkhorst-Pack  $k$ -point mesh of size  $12 \times 12 \times 12$ , and the total energy difference criterion was defined as  $10^{-6}$  eV for self-consistent convergence. The GGA +  $U$  scheme was utilized to consider the effect of Coulomb repulsion in the Eu  $4f$  orbital.

## II. RESULTS AND DISCUSSION

The resistivity and magnetic properties of  $\text{EuB}_6$  are depicted in Figs. 1(a) and 1(b), respectively. Seen from the temperature dependence of longitudinal resistivity  $\rho_{xx}$  at magnetic field  $B = 0$  T with the current  $I//[100]$  direction presented in Fig. 1(a), below 100 K, it gradually increases with cooling temperature to  $\sim 12$  K, and subsequently exhibits a sudden drop with further decreasing the temperature to 2 K, consistent with the FM phase transition manifested by magnetic susceptibility presented in the inset of Fig. 1(b). Therefore, the Kondo-like increase of resistivity should be ascribed to the enhanced scattering of conduction carriers from the Eu magnetic moment due to the critical magnetic fluctuations approaching the ferromagnetic phase, and the formation of magnetic order will then reduce the scattering, leading to the rapid decrease of  $\rho_{xx}$ .

The magnetic field dependence of the magnetizations along the three directions of  $M//[001]$ ,  $[110]$ , and  $[111]$  at 2 K are presented in Fig. 1(b). It should be noted that the magnetization is zero at  $B \sim 0$  T, which confirms that  $\text{EuB}_6$  is a soft magnetic material. In previous reports, the simultaneous formation of magnetic domains has been observed by magneto-optical Kerr effect microscopy, implying the intimate link between the topological phase transition and broken time-reversal symmetry [31]. Therefore, we suppose

that the nearly zero magnetic moment in the magnetic ground state is due to the opposite directions of magnetizations in different magnetic domains. By increasing  $B$ , the FM order is apparently enhanced with the saturation moment at 2 K close to  $7\mu_B$ , suggesting that spins of the localized Eu  $4f^7$  electrons are actually fully polarized along the magnetic field direction, as shown in Fig. 1(c), and the system eventually enters into the spin-polarized state. Meanwhile, we can see that there are two mirror symmetries  $M_z$  and  $M_{[110]}$  in the  $M//[001]$  and  $M//[110]$  directions, respectively. In contrast, there is no mirror symmetry with the  $M//[111]$  direction. In the inset of Fig. 1(b), we see that for  $B = 0.01$  T, the magnetization along the  $[001]$  direction in the ordered state is larger than those along the  $[110]$  and  $[111]$  directions, which implies that the easy axis may be along the  $[001]$  direction. The isothermal magnetizations at different temperatures for the three magnetization directions are presented in Fig. 2.

We continue to discuss the electronic band structures corresponding to the different ferromagnetic states with  $M$  along the  $[001]$ ,  $[110]$ , and  $[111]$  directions. As shown in Fig. 3(a), the calculated FM band structure of  $\text{EuB}_6$  without SOC displays half-semimetallic behavior. The bands in the spin-down channel exhibit a semiconducting character with a gap of 0.1 eV, whereas the spin-up channel shows a semimetallic feature with the conduction band being crossed with the valence band. In the presence of SOC, if  $M$  is along the  $[001]$  axis,  $\text{EuB}_6$  is a Weyl type nodal-line semimetal with two nodal rings centered at the  $X$  and  $Y$  points of the Brillouin zone in the  $k_z = 0$  plane and one nodal ring centered at the  $Z$  point in the  $k_z = \pi$  plane, which are protected by the mirror symmetry  $M_z$  as shown in Fig. 1(c). The nodal lines are schematically plotted in the inset of Fig. 3(b). Once the  $M$  orientation is changed from  $[001]$  to the  $[110]$  axis by a weak external magnetic field, the nodal rings in the  $M//[001]$  phase will be gapped due to the breaking of mirror symmetry  $M_z$ , generating two pairs of Weyl points in the  $k_z = 0$  plane. In addition to the Weyl points, there is a nodal ring centered at the  $Z$  point in the vertical diagonal mirror plane, i.e., the  $M_{[110]}$  plane, as schematically shown in the inset of Fig. 3(c).  $\text{EuB}_6$  thus is a topological semimetal hosting both Weyl fermions and nodal-line fermions when  $M$  is along the  $[110]$  direction. Figure 3(d) shows the electronic structure of  $\text{EuB}_6$  when  $M//[111]$ , in which there are three

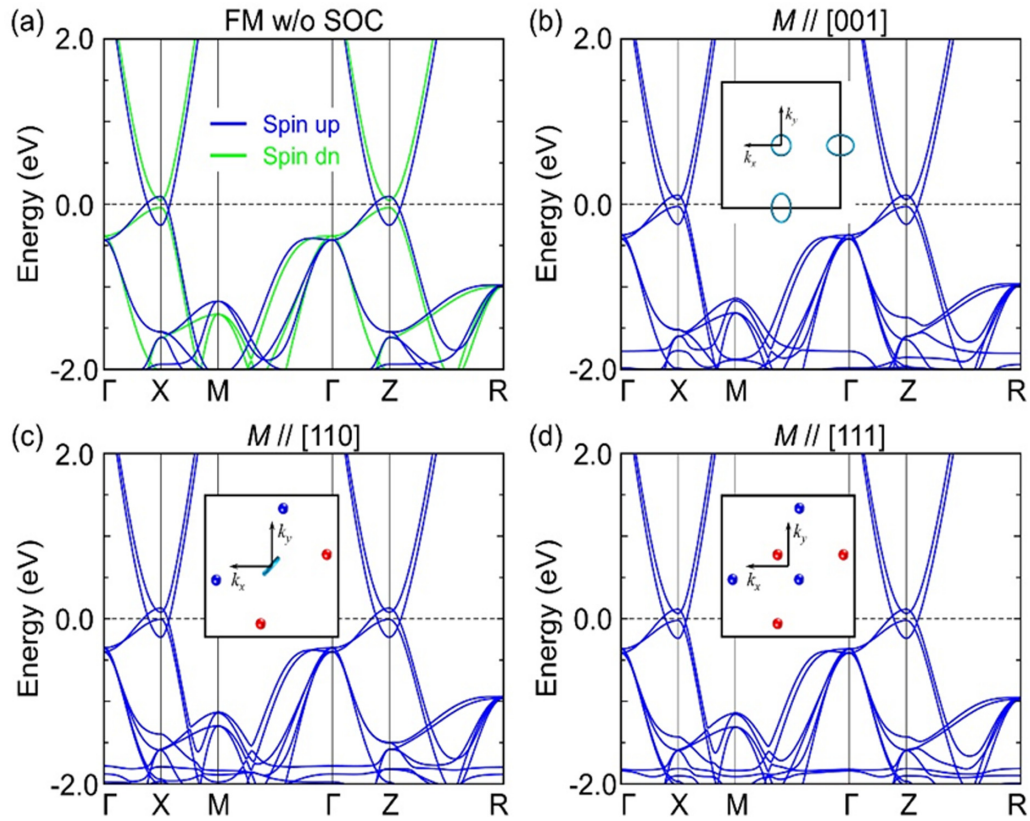


FIG. 3. (a) Spin-resolved band structure for the FM state of  $\text{EuB}_6$  from GGA +  $U$  ( $U = 8 \text{ eV}$ ) calculations. Band structures calculated using GGA +  $U$  + SOC ( $U = 8 \text{ eV}$ ) for FM states with the  $M$  orientations along the (b) [001], (c) [110], and (d) [111] directions. Insets in [(b)–(d)] illustrate the projections of the nodal line (indicated by the cyan lines) configurations and Weyl point (labeled by red/blue dots with different chiralities) distribution on the (001) surface Brillouin zone.

pairs of Weyl nodes owing to the breaking of all mirror symmetries of the system. The distributions of these Weyl points in the  $M//[111]$  phase are schematically shown in the inset of Fig. 3(d). To clearly show the effects of spin configurations on the electronic band structure, we calculated the detailed

band structures around the  $X$  and  $Z$  points of the Brillouin zone for the three FM phases, as presented in Fig. 4. When  $M//[001]$ , the valence and conduction bands cross along the  $\Gamma-X$ ,  $X-M$ , and  $Z-R$  high symmetry lines, while along the  $\Gamma-Z$  line, there is a tiny band gap between the valence and

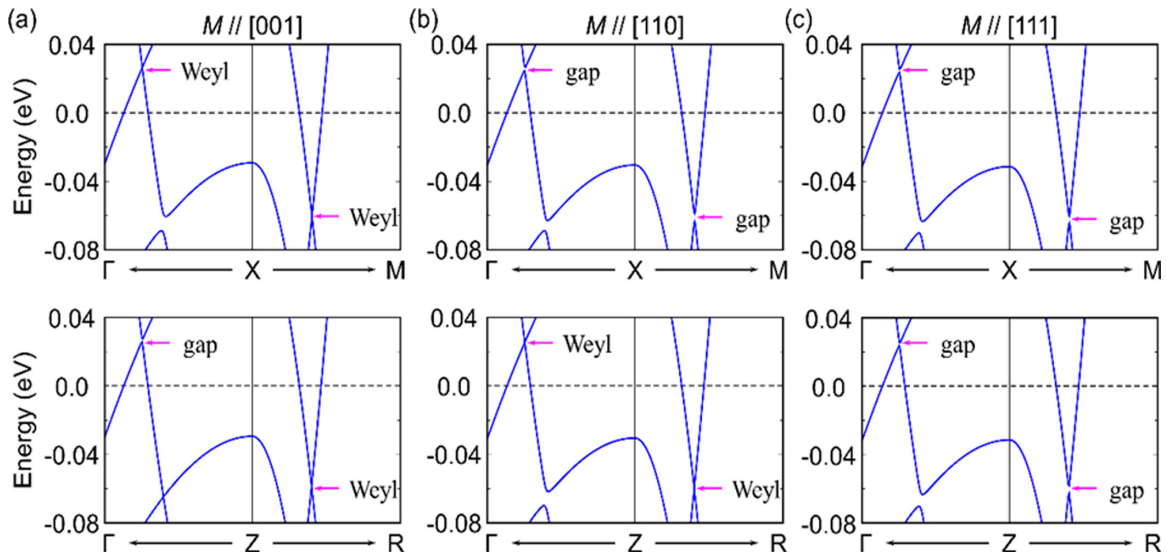


FIG. 4. The band structures around the  $X$  and  $Z$  points calculated by using GGA +  $U$  + SOC ( $U = 8 \text{ eV}$ ) for FM states with spin orientation along the (a) [001], (b) [110], and (c) [111] directions.

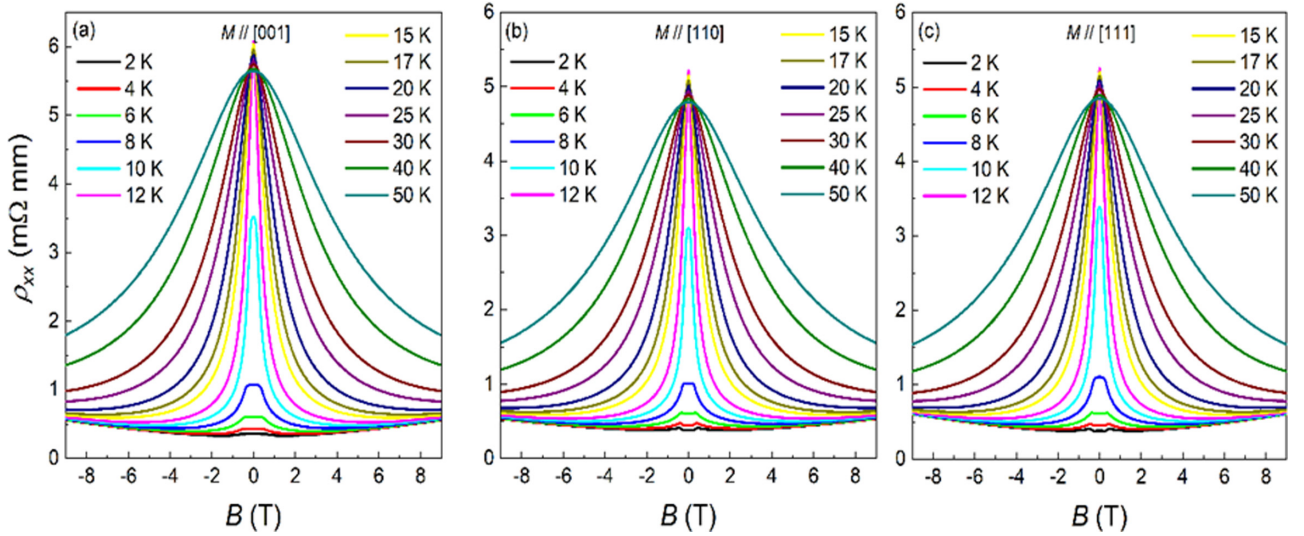


FIG. 5. (a)–(c) the longitudinal resistivity at different temperatures with  $M//[001]$ ,  $M//[110]$ , and  $M//[111]$ , respectively.

conduction bands. In fact, the band crossing points on the  $\Gamma-X$  and  $X-M$  lines are residing on a nodal ring centered at the  $X$  point in the  $k_z = 0$  plane, and the band crossing point on the  $Z-R$  line is residing on a nodal ring centered at the  $Z$  point in the  $k_z = \pi$  plane. When  $M//[110]$ , the band crossing points on the  $\Gamma-X$  and  $X-M$  lines are gapped out due to the breaking of the  $M_z$  mirror symmetry, while along the  $\Gamma-Z$  and  $Z-R$  lines, the valence and conduction bands cross each other. The reason why the band crossing points on the  $\Gamma-Z$  and  $Z-R$  lines survive is that there is a nodal ring centered at the  $Z$  point in the  $M_{xy}$  mirror plane. When  $M//[111]$ , all the band crossing points on the  $\Gamma-X$ ,  $X-M$ ,  $\Gamma-Z$ , and  $Z-R$  lines are gapped out due to the breaking of all mirror symmetries.

We turn to a discussion of the magnetotransport properties of  $\text{EuB}_6$  in different magnetic configurations. The temperature and magnetic field dependent longitudinal resistivities for  $M$  along the [001], [110], and [111] directions are presented in Fig. 5. Figure 6(a) shows the magnetic field dependence of longitudinal resistivity  $\rho_{xx}$  at different rotation angles at 2 K and Fig. 6(b) illustrates the geometry for rotation measurements. At  $\theta = 0^\circ$ , i.e., the  $B//[110]$  direction, there is a resistivity plateau for weak magnetic field  $B < B_L$ , where  $B_L$  is the threshold magnetic field at which the  $\rho_{xx}$  starts to increase, which is commonly observed in some AFM materials with spin-flop transition [12,41]. By increasing  $B$ , the scattering between carriers and magnetic moments is enhanced due to the spin-reorientation transition, leading to the increase of resistivity. Thus, the maximum resistivity corresponds to the strongest scattering at  $B \approx B_H$  due to the maximized magnetic fluctuations around the transition point. Here  $B_H$  can be considered as a critical magnetic field at which the spin reorientation occurs. When  $B > B_H$ , the magnetization is reoriented by the magnetic field; thus the reduced magnetic fluctuations diminish the resistivity induced by the scattering between electrons and magnetism. The resistivity plateau is preserved until  $\theta = 37^\circ$ , i.e., the  $B//[111]$  direction, where the difference between  $\rho_H$  and  $\rho_L$ , i.e.,  $\rho_H - \rho_L$ , reaches the maximum as shown in Fig. 6(c), indicating that the largest scattering-induced variation of magnetoresistivity occurs at

this angle. When the angle is further increased, the negative magnetoresistance emerges at  $B < B_L$  and it is also accompanied by the decrease of the  $\rho_H - \rho_L$ . Until the angle reaches  $90^\circ$ , i.e., the  $B//[001]$  direction, the spin reorientation induced abrupt enhancement in the magnetoresistance disappears, and instead a complete negative magnetoresistance behavior shows up. Such anisotropic magnetotransport behavior indicates that the magnetization tends to be aligned along the [001] direction and other symmetry-equivalent directions, which is coincident with the theoretic calculations presented in Table I. When  $B$  is oriented to the [001] direction, the number of magnetic domains in the system is gradually decreased with a gradual increase in the magnetization along [001], resulting in the continuous decrease of resistivity due to the suppressed scattering between electrons and magnetic domain walls. Once the magnetic field is oriented to the [110] or [111] direction, or to a direction deviated from [001], the magnetization along [001] remains robust for weak magnetic fields due to the magnetocrystalline anisotropy, unless the magnetic field exceeds the threshold field  $B_L$ , which drives a spin-reorientation transition. This explains the emergence of the resistivity plateaus for  $B < B_L$ , as well as the abrupt enhancement of resistivity when  $B \sim B_L$ . The magnetotransport properties show that the magnetic anisotropy of  $\text{EuB}_6$  has a large influence on the transport, which allows the characterization of the topological states in different directions by measuring the transport properties.

It is well known that WSMs with broken time-reversal symmetry, i.e., magnetic WSMs, are also characterized by

TABLE I. The calculated total energies of different FM phases. The total energy of the  $M//[001]$  state is chosen as the reference to show the energy difference among different phases.

Phase (meV/f.u.)	$M//[001]$	$M//[110]$	$M//[111]$
Total energy	-53607.47110	-53607.46957	-53607.46933
Energy difference	0	0.0015	0.0018

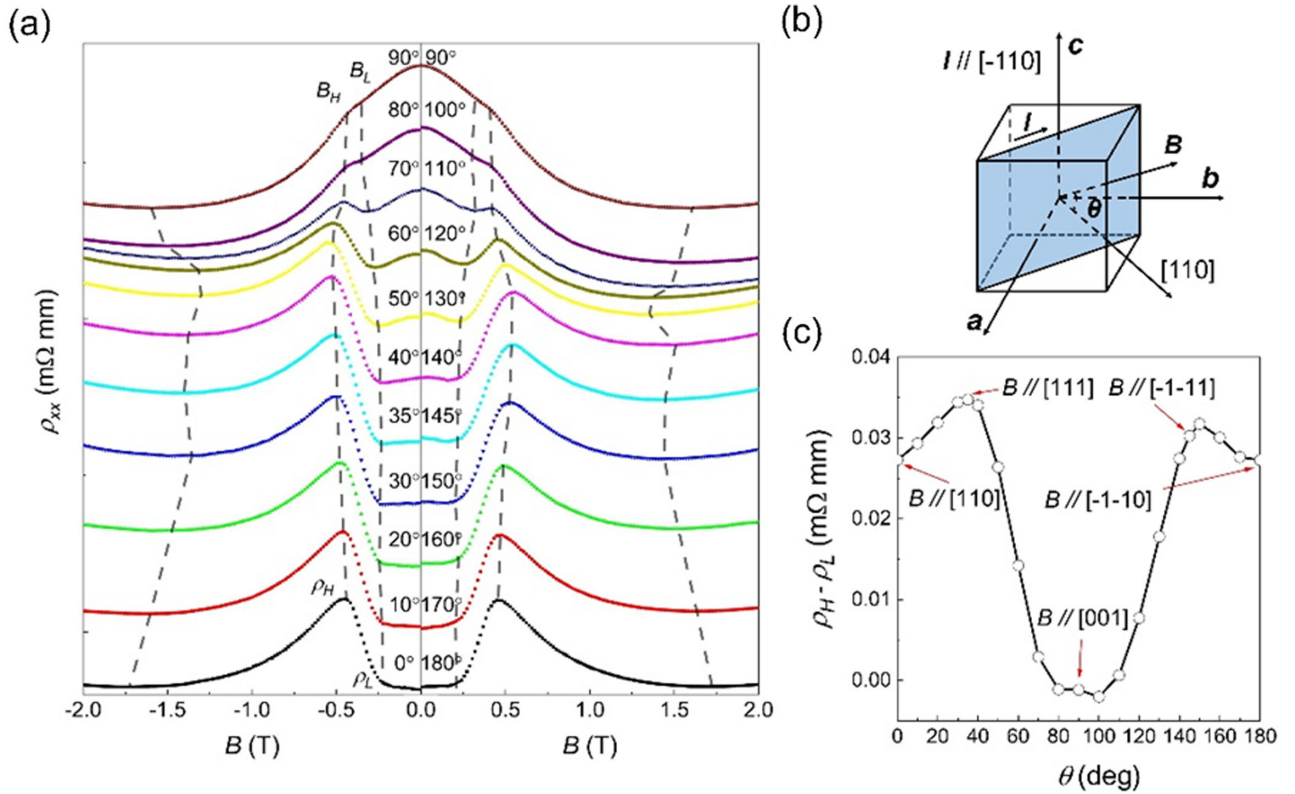


FIG. 6. (a) Longitudinal resistivity  $\rho_{xx}$  versus magnetic field  $B$  at different angles and at the temperature of 2 K. (b) Schematic geometry for the magnetic field rotation measurements. The blue plane is (110), the orange plane is  $(-110)$ , and  $\theta$  highlighted by red is the angle between  $B$  and [110]. (c) Difference between  $\rho_H$  and  $\rho_L$  versus angles signifying the scattering between carriers and magnetism during the spin-reorientation transition.

notable anomalous Hall effect (AHE) [58–62]. The Weyl nodes characterizing the WSMs can be regarded as “magnetic monopoles” in momentum space, which are the sources generating Berry curvatures in the Brillouin zone. When the Weyl nodes are close to the Fermi level  $E_F$ , they would contribute to giant net Berry curvature, and generate large intrinsic AHE, which is generally recognized as a fingerprint of the presence of Weyl nodes in a magnetic metallic system. To probe the predicted Weyl state in the FM states of  $\text{EuB}_6$ , the field dependence of the anomalous Hall resistivities  $\rho_{xy}^A$  have been extracted and are displayed in Figs. 7(a)–7(c) for  $M//[001]$ ,  $M//[110]$ , and  $M//[111]$ , respectively, in the magnetic field range of  $-9$  to  $0$  T, and the data which are apparently symmetric with respect to the measured magnetic field directions in the whole magnetic field range from  $-9$  to  $9$  T are presented in Fig. 5. Figure 8 shows the transverse resistivities for  $M//[001]$ ,  $M//[110]$ , and  $M//[111]$ , respectively, of  $\text{EuB}_6$  at various temperatures, which are basically nonlinear in the temperature range of  $2$ – $20$  K. Thus, to expose the carriers for transport, we used the two-band model [63] to fit the data, which is expressed as

$$\sigma_{xy} = \left[ \frac{n_h \mu_h^2}{1 + (\mu_h B)^2} - \frac{n_e \mu_e^2}{1 + (\mu_e B)^2} \right] eB,$$

where  $n_e(n_h)$  denotes the carrier density for the electron (hole), and  $\mu_e(\mu_h)$  is the mobility of the electron (hole), respectively. The fit is fairly nice at the high field part in the spin-polarized state. Figures 8(d)–8(f) show the fitting results

at 2 K with  $M//[001]$ ,  $M//[110]$ , and  $M//[111]$ , respectively. After subtracting the two-band model fitting part indicated in Figs. 8(d)–8(f), the anomalous Hall resistivity was obtained, which is shown in Fig. 9.

However, in a magnetic topological system, it is necessary to trace the origin of the AHE since other extrinsic sources such as skew and side-jump contributions besides the Berry curvature could also produce AHE [64]. To determine the dominant mechanism for the AHE, the so-called TYJ (Tian-Ye-Jin) scaling method was used [65], which has been demonstrated to be effective in an array of previous works [60,61,66,67]. Within the framework of the TYJ scaling method, the total Hall resistivity can be expressed as  $\rho_{xy} = \rho_{xy}^N + \rho_{xy}^A = R_0 B + R_s 4\pi M$ , where  $R_0$  is the normal Hall coefficient, and  $R_s$  is the anomalous Hall coefficient. A more specific formula of  $\rho_{xy}^A$  including the longitudinal resistivity is  $\rho_{xy}^A = a(M)\rho_{xx} + b(M)\rho_{xx}^2$ , where the first term denotes the extrinsic contributions including the skew component, while the second term represents the intrinsic contributions also including the side-jump component [68].

Therefore, according to the above formula,  $\frac{\rho_{xy}^A}{M\rho_{xx}} = b\rho_{xx}$  is from intrinsic contribution from the spin-polarized states. As shown in Figs. 7(d)–7(f),  $\rho_{xy}^A/(M\rho_{xx})$  are all linearly dependent on  $\rho_{xx}$  when  $\rho_{xx} < 0.95$  mΩ mm in three different spin-polarized states, suggesting that the dominant contribution to AHE in  $\text{EuB}_6$  is from the intrinsic Berry curvatures of the band structures. At 2 K, the converted anomalous Hall

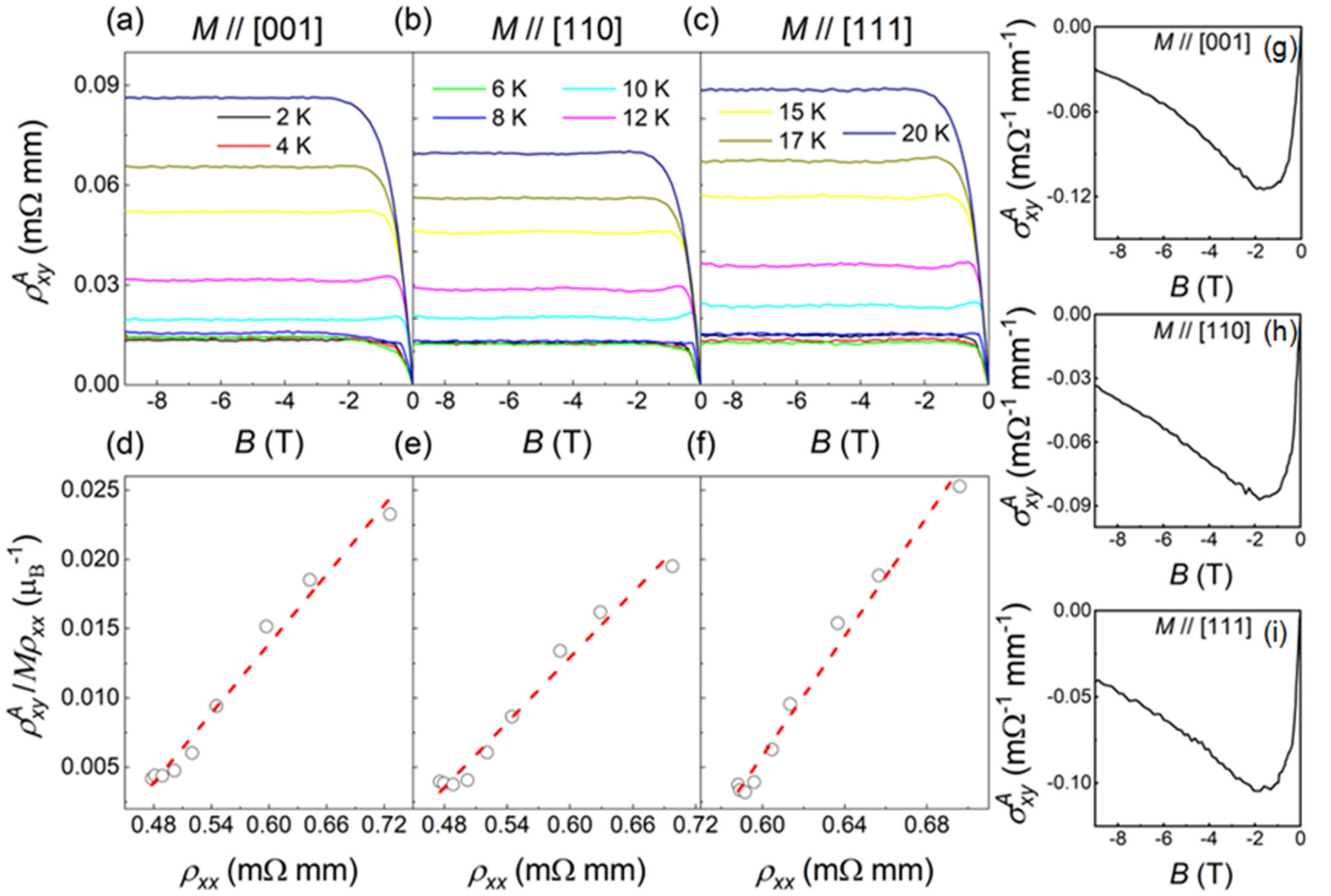


FIG. 7. (a)–(c) Anomalous Hall resistivities  $\rho_{xy}^A$  versus magnetic field at various temperatures. (d)–(f)  $\rho_{xy}^A/(M\rho_{xx})$  versus  $\rho_{xx}$ , where the red dashed line denotes the linear fit. [(g)–(i)] Anomalous Hall conductivities  $\sigma_{xy}^A$  versus magnetic field at 2 K for  $M//[001]$ ,  $M//[110]$ , and  $M//[111]$ , respectively.

conductivities (AHCs)  $\sigma_{xy}^A = -\rho_{xy}^A/[(\rho_{xy}^A)^2 + \rho_{xx}^2]$  are presented in Figs. 7(g)–7(i). The  $\sigma_{xy}^A$  is extracted to be  $\sim 0.03 \text{ m}\Omega^{-1} \text{ mm}^{-1}$  in all ferromagnetic states, which is rather close to the theoretical values of  $\sim 0.015\text{--}0.02 \text{ m}\Omega^{-1} \text{ mm}^{-1}$  as discussed in Ref. [33]. On the other side, the side-jump contribution  $\sigma_{xy,sj}^A$  can be estimated by the expression  $e^2/(ha)(\varepsilon_{\text{SOC}}/E_F)$ , where  $\varepsilon_{\text{SOC}}$  is the SOC energy [69,70]. Taking the lattice constant  $a \sim 4.185 \text{ \AA}$  and  $\varepsilon_{\text{SOC}}/E_F \sim 0.01$  for metallic ferromagnet EuB<sub>6</sub>, the  $|\sigma_{xy,sj}^A|$  was estimated as  $9.23 \times 10^{-4} \text{ m}\Omega^{-1} \text{ mm}^{-1}$ , which is almost negligible, thus demonstrating that the AHCs are mainly contributed by the Berry curvatures.

To distinguish the topological states with magnetizations along the [001], [110], and [111] directions, our calculations presented in Table II indicate that the AHCs in the three different ferromagnetic states actually have different magnitudes. According to our calculations, the AHCs in three directions are apparently distinguishable; they are  $\Delta\sigma_{[110],[001]}^A \sim 0.003 \text{ m}\Omega^{-1} \text{ mm}^{-1}$  and  $\Delta\sigma_{[111],[001]}^A \sim 0.011 \text{ m}\Omega^{-1} \text{ mm}^{-1}$ . So,  $\Delta\sigma_{[111],[001]}^A$  is nearly 4 times  $\Delta\sigma_{[110],[001]}^A$  and  $\Delta\sigma_{[111],[001]}^A$  is approximately 1/3 of  $\sigma_{[001]}^A$  ( $\sim 0.03 \text{ m}\Omega^{-1} \text{ mm}^{-1}$ ). To provide some in-depth insight into the AHCs of the different directions, the intrinsic AHC  $\sigma_{xy,in}^A$  versus magnetization with  $M//[001]$ ,  $M//[110]$ , and  $M//[111]$  at 2 K are pre-

sented in Fig. 10, which clearly shows that  $\sigma_{xy,in}^A$  is linearly proportional to  $M$ , nicely consistent with the result in Ref. [65]. The derived largest intrinsic AHCs are 0.063, 0.148, and  $0.205 \text{ m}\Omega^{-1} \text{ mm}^{-1}$ , respectively, for  $M//[001]$ ,  $M//[110]$ , and  $M//[111]$ . It is apparent that  $\sigma_{xy,in}^A$  at  $M//[111]$  is larger than those of  $M//[001]$  and  $M//[110]$ . It should be noted that the existence of mirror symmetries  $M_Z$  and  $M_{[110]}$  protects the nodal rings and leads to a small difference of the (intrinsic) AHCs between  $M//[001]$  and  $M//[110]$ , while the entire mirror symmetry breaking that generates the three pairs of Weyl points contributes more significantly to (intrinsic) AHCs. Therefore the difference of AHCs and intrinsic

TABLE II. The AHCs and intrinsic AHCs for  $M//[001]$ ,  $M//[110]$ , and  $M//[111]$  together with their difference at 2 K.

AHC( $\text{m}\Omega^{-1} \text{ mm}^{-1}$ )	$M//[001]$ (M1)	$M//[110]$ (M2)	$M//[111]$ (M3)
$\sigma_{xy}^A$	0.030	0.033	0.041
$\sigma_{xy,in}^A$	0.063	0.148	0.205
$ \Delta\sigma_{xy}^A(M1, M2) $	0.003	$ \Delta\sigma_{xy}^A(M1, M3) $	0.011
$ \Delta\sigma_{xy,in}^A(M1, M2) $	0.085	$ \Delta\sigma_{xy,in}^A(M1, M3) $	0.142

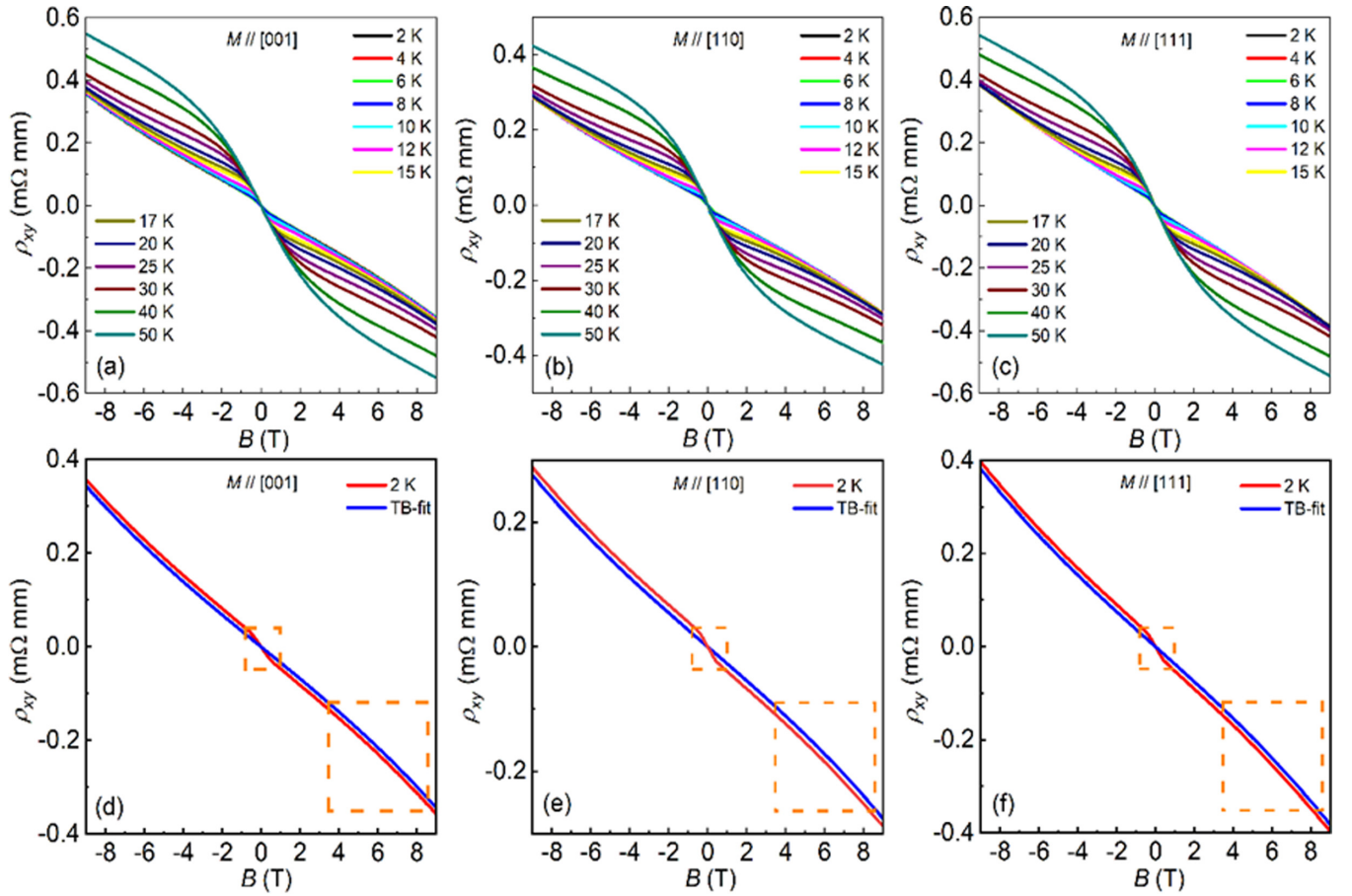


FIG. 8. (a)–(c) Transverse resistivity at different temperatures with  $M // [001]$ ,  $M // [110]$ , and  $M // [111]$ , respectively. (d)–(f) The fitting results by using the two-band model at 2 K. The large dashed frame zone is the fit part and the small dashed frame shows a deviation.

AHCs could guarantee the tunability of the Weyl states along different directions seen in Fig. 4.

### III. SUMMARY

In summary, the magnetocrystalline anisotropy and the relatively strong coupling between the local magnetization and the conduction electrons in  $\text{EuB}_6$  allow for a direct in-

vestigation of the topological properties via measuring the magnetotransport properties. With the aid of the first principles calculations, the measurements unveiled that  $\text{EuB}_6$  actually hosts versatile magnetic topological phases along different crystallographic directions due to the varied magnetizations, thus exposing the intimate correlation between them. The results would be very instructive for the study of magnetic topological physics, in particular, in such type of

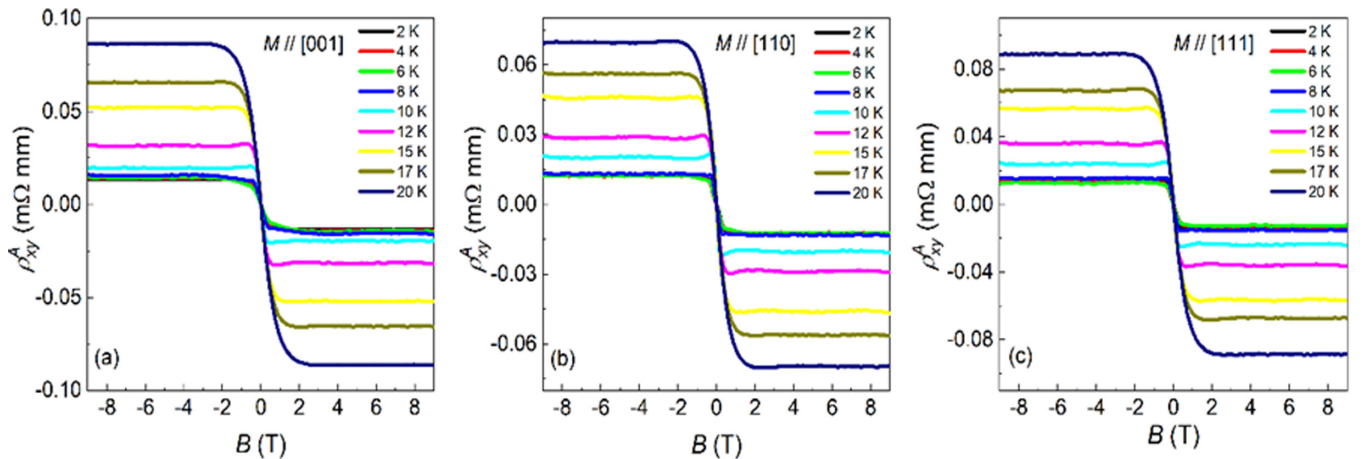


FIG. 9. The anomalous Hall resistivities with  $M // [001]$ ,  $M // [110]$ , and  $M // [111]$  in the temperature range of 2–20 K.

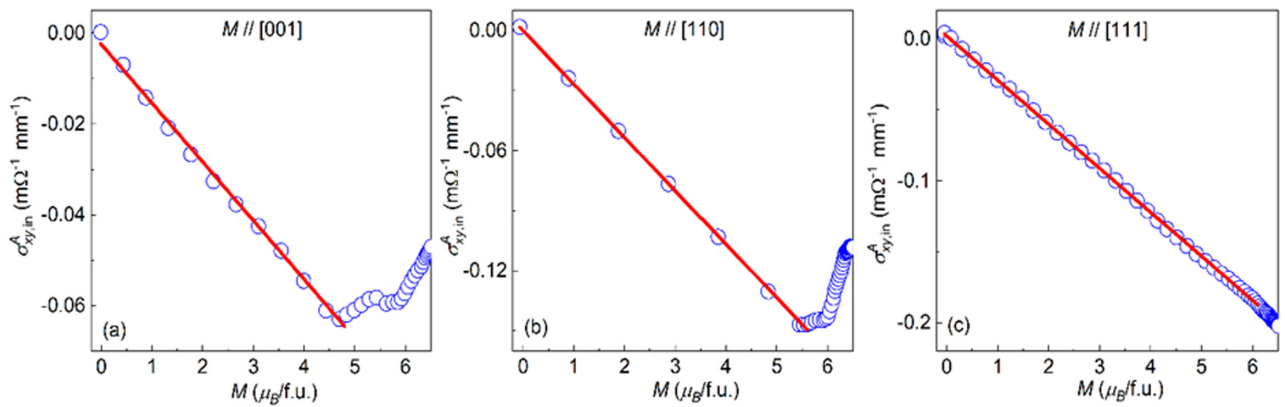


FIG. 10. The intrinsic anomalous Hall conductivities as a function of magnetization with  $M//[001]$ ,  $M//[110]$ , and  $M//[111]$  at 2 K.

topological phases with strong magnetic anisotropy. Moreover, the tunable Weyl states in a single material provide an excellent candidate for use in topological devices with versatile functionalities. According to the theoretical prediction [32], large Chern number quantum anomalous Hall effect could be realized in its [111]-oriented quantum-well structures of  $\text{EuB}_6$ . The present study would pave the way toward the realization of the exotic topological properties.

#### ACKNOWLEDGMENTS

The authors acknowledge the support from the National Natural Science Foundation of China (Grants No. 92065201

and No. 11874264) and the Shanghai Science and Technology Innovation Action Plan (Grant No. 21JC1402000). J.L. acknowledges the start-up grant of ShanghaiTech University and the National Key R & D program of China (Grant No. 2020YFA0309601). Y.G. acknowledges the start-up grant of ShanghaiTech University and the Program for Professor of Special Appointment (Shanghai Eastern Scholar). W.Z. is supported by the Shenzhen Peacock Team Plan (Grant No. KQTD20170809110344233) and Bureau of Industry and Information Technology of Shenzhen through the Graphene Manufacturing Innovation Center (Grant No. 201901161514). The authors also acknowledge the support from the Analytical Instrumentation Center (Grant No. SPST-AIC10112914), SPST, ShanghaiTech University.

- 
- [1] Z. L. Liao, P. H. Jiang, Z. C. Zhong, and R. W. Li, *npj Quantum Mater.* **5**, 30 (2020).
- [2] J. H. Li, Y. Li, S. Q. Du, Z. Wang, B. L. Gu, S. C. Zhang, K. He, W. H. Duan, and Y. Xu, *Sci. Adv.* **5**, eaaw5685 (2019).
- [3] Y. J. Chen, L. X. Xu, J. H. Li, Y. W. Li, H. Y. Wang, C. F. Zhang, H. Li, Y. Wu, A. J. Liang, C. Chen, S. W. Jung, C. Cacho, Y. H. Mao, S. Liu, M. X. Wang, Y. F. Guo, Y. Xu, Z. K. Liu, L. X. Yang, and Y. L. Chen, *Phys. Rev. X* **9**, 041040 (2019).
- [4] Y. Gong, J. W. Guo, J. H. Li, K. J. Zhu, M. H. Liao, X. Z. Liu, Q. H. Zhang, L. Gu, L. Tang, X. Feng, D. Zhang, W. Li, C. L. Song, L. L. Wang, P. Yu, X. Chen, Y. Y. Wang, H. Yao, W. H. Duan, Y. Xu *et al.*, *Chin. Phys. Lett.* **36**, 076801 (2019).
- [5] H. Li, S. Y. Gao, S. F. Duan, Y. F. Xu, K. J. Zhu, S. J. Tian, J. C. Gao, W. H. Fan, Z. C. Rao, J. R. Huang, J. J. Li, D. Y. Yan, Z. T. Liu, W. L. Liu, Y. B. Huang, Y. L. Li, Y. Liu, G. B. Zhang, P. Zhang, T. Kondo *et al.*, *Phys. Rev. X* **9**, 041039 (2019).
- [6] Y. J. Hao, P. F. Liu, Y. Feng, X. M. Ma, E. F. Schwier, M. Arita, S. Kumar, C. W. Hu, R. Lu, M. Zeng, Y. Wang, Z. Y. Hao, H. Y. Sun, K. Zhang, J. W. Mei, N. Ni, L. S. Wu, K. Shimada, C. Y. Chen, Q. H. Liu *et al.*, *Phys. Rev. X* **9**, 041038 (2019).
- [7] M. M. Otrokov, I. I. Klimovskikh, H. Bentmann, D. Estyunin, A. Zeugner, Z. S. Aliev, S. Gaß, A. U. B. Wolter, A. V. Koroleva, A. M. Shikin, M. Blanco-Rey, M. Hoffmann, I. P. Rusinov, A. Yu. Vyazovskaya, S. V. Eremeev, Yu. M. Koroteev, V. M. Kuznetsov, F. Freyse, J. Sánchez-Barriga, I. R. Amiraslanov *et al.*, *Nature (London)* **576**, 416 (2019).
- [8] E. D. L. Rienks, S. Wimmer, J. Sánchez-Barriga, O. Caha, P. S. Mandal, J. Růžicka, A. Ney, H. Steiner, V. V. Volobuev, H. Groiss, M. Albu, G. Kothleitner, J. Michalička, S. A. Khan, J. Minár, H. Ebert, G. Bauer, F. Freyse, A. Varykhalov *et al.*, *Nature (London)* **576**, 423 (2019).
- [9] C. Liu, Y. C. Wang, H. Li, Y. Wu, Y. X. Li, J. H. Li, K. He, Y. Xu, J. S. Zhang, and Y. Y. Wang, *Nat. Mater.* **19**, 522 (2020).
- [10] D. Q. Zhang, M. J. Shi, T. S. Zhu, D. Y. Xing, H. J. Zhang, and J. Wang, *Phys. Rev. Lett.* **122**, 206401 (2019).
- [11] Y. J. Deng, Y. J. Yu, M. Z. Shi, Z. X. Guo, Z. H. Xu, J. Wang, X. H. Chen, and Y. B. Zhang, *Science* **367**, 895 (2020).
- [12] J. Q. Yan, S. Okamoto, M. A. McGuire, A. F. May, R. J. McQueeney, and B. C. Sales, *Phys. Rev. B* **100**, 104409 (2019).
- [13] J. P. Liu and L. Balents, *Phys. Rev. Lett.* **119**, 087202 (2017).
- [14] J. X. Yin, S. T. S. Zhang, H. Li, K. Jiang, G. Q. Chang, B. J. Zhang, B. Lian, C. Xiang, I. Belopolski, H. Zheng, T. A. Cochran, S. Y. Xu, G. Bian, K. Liu, T. R. Chang, H. Lin, Z. Y. Lu, Z. Q. Wang, S. Jia, W. H. Wang *et al.*, *Nature (London)* **562**, 91 (2018).
- [15] M. Yao, H. Lee, N. Xu, Y. Wang, J. Ma, O. V. Yazyev, Y. Xiong, M. Shi, G. Aeppli, and Y. Soh, *arXiv:1810.01514*.

- [16] H. M. Weng, J. Z. Zhao, Z. J. Wang, Z. Fang, and X. Dai, *Phys. Rev. Lett.* **112**, 016403 (2014).
- [17] F. Lu, J. Z. Zhao, H. M. Weng, Z. Fang, and X. Dai, *Phys. Rev. Lett.* **110**, 096401 (2013).
- [18] Y. Ohtsubo, Y. Yamashita, K. Hagiwara, S.-I. Ideta, K. Tanaka, R. Yukawa, K. Horiba, H. Kumigashira, K. Miyamoto, T. Okuda, W. Hirano, F. Iga, and S.-I. Kimura, *Nat. Commun.* **10**, 2298 (2019).
- [19] N. Xu, C. E. Matt, E. Pomjakushina, J. H. Dil, G. Landolt, J. Z. Ma, X. Shi, R. S. Dhaka, N. C. Plumb, M. Radovic, V. N. Strocov, T. K. Kim, M. Hoesch, K. Conder, J. Mesot, H. Ding, and M. Shi, [arXiv:1405.0165](https://arxiv.org/abs/1405.0165).
- [20] C. J. Kang, J. D. Denlinger, J. W. Allen, C. H. Min, F. Reinert, B. Y. Kang, B. K. Cho, J. S. Kang, J. H. Shim, and B. I. Min, *Phys. Rev. Lett.* **116**, 116401 (2016).
- [21] M. Neupane, S. Y. Xu, N. Alidoust, G. Bian, D. J. Kim, C. Liu, I. Belopolski, T. R. Chang, H. T. Jeng, T. Durakiewicz, H. Lin, A. Bansil, Z. Fisk, and M. Z. Hasan, *Phys. Rev. Lett.* **114**, 016403 (2015).
- [22] L. Li, K. Sun, C. Kurdak, and J. W. Allen, *Nat. Rev. Phys.* **2**, 463 (2020).
- [23] C. N. Guy, S. von Molnar, J. Etourneau, and Z. Fisk, *Solid State Commun.* **33**, 1055 (1980).
- [24] P. Nyhus, S. Yoon, M. Kauffman, S. L. Cooper, Z. Fisk, and J. Sarrao, *Phys. Rev. B* **56**, 2717 (1997).
- [25] L. Degiorgi, E. Felder, H. R. Ott, J. L. Sarrao, and Z. Fisk, *Phys. Rev. Lett.* **79**, 5134 (1997).
- [26] S. Broderick, B. Ruzicka, L. Degiorgi, H. R. Ott, J. L. Sarrao, and Z. Fisk, *Phys. Rev. B* **65**, 121102(R) (2002).
- [27] S. Süllow, I. Prasad, M. C. Aronson, S. Bogdanovich, J. L. Sarrao, and Z. Fisk, *Phys. Rev. B* **62**, 11626 (2000).
- [28] B. Amsler, Z. Fisk, J. L. Sarrao, S. von Molnar, M. W. Meisel, and F. Sharifi, *Phys. Rev. B* **57**, 8747 (1998).
- [29] S. Süllow, I. Prasad, M. C. Aronson, J. L. Sarrao, Z. Fisk, D. Hristova, A. H. Lacerda, M. F. Hundley, A. Vigliante, and D. Gibbs, *Phys. Rev. B* **57**, 5860 (1998).
- [30] M. L. Brooks, T. Lancaster, S. J. Blundell, W. Hayes, F. L. Pratt, and Z. Fisk, *Phys. Rev. B* **70**, 020401(R) (2004).
- [31] W. L. Liu, X. Zhang, S. M. Nie, Z. T. Liu, X. Y. Sun, H. Y. Wang, J. Y. Ding, L. Sun, Z. Huang, H. Su, Y. C. Yang, Z. C. Jiang, X. L. Lu, J. S. Liu, Z. H. Liu, S. L. Zhang, H. M. Weng, Y. F. Guo, Z. J. Wang, D. W. Shen *et al.*, [arXiv:2103.04658](https://arxiv.org/abs/2103.04658).
- [32] S. Y. Gao, S. Xu, H. Li, C. J. Yi, S. M. Nie, Z. C. Rao, H. Wang, Q. X. Hu, X. Z. Chen, W. H. Fan, J. R. Huang, Y. B. Huang, N. Pryds, M. Shi, Z. J. Wang, Y. G. Shi, T. L. Xia, T. Qian, and H. Ding, *Phys. Rev. X* **11**, 021016 (2021).
- [33] S. M. Nie, Y. Sun, F. B. Prinz, Z. J. Wang, H. M. Weng, Z. Fang, and X. Dai, *Phys. Rev. Lett.* **124**, 076403 (2020).
- [34] J. L. Shen, J. C. Gao, C. J. Yi, Q. Q. Zeng, S. Zhang, J. Y. Yang, X. D. Zhang, B. B. Wang, J. Z. Cong, Y. G. Shi, X. H. Xu, Z. J. Wang, and E. K. Liu, [arXiv:2106.02904](https://arxiv.org/abs/2106.02904).
- [35] W. Ko, M. Kolmer, J. Yan, A. D. Pham, M. Fu, F. Lüpke, S. Okamoto, Z. Gai, P. Ganesh, and A.-P. Li, *Phys. Rev. B* **102**, 115402 (2020).
- [36] H. Su, B. C. Gong, W. J. Shi, H. F. Yang, H. Y. Wang, W. Xia, Z. Y. Yu, P. J. Guo, J. H. Wang, L. C. Ding, L. C. Xu, X. K. Li, X. Wang, Z. Q. Zou, N. Yu, Z. W. Zhu, Y. L. Chen, Z. K. Liu, K. Liu, G. Li *et al.*, *APL Mater.* **8**, 011109 (2020).
- [37] J.-R. Soh, F. de Juan, M. G. Vergniory, N. B. M. Schröter, M. C. Rahn, D. Y. Yan, J. Jiang, M. Bristow, P. Reiss, J. N. Blandy, Y. F. Guo, Y. G. Shi, T. K. Kim, A. McCollam, S. H. Simon, Y. Chen, A. I. Coldea, and A. T. Boothroyd, *Phys. Rev. B* **100**, 201102(R) (2019).
- [38] S. H. Liang, J. J. Lin, S. Kushwaha, J. Xing, N. Ni, R. J. Cava, and N. P. Ong, *Phys. Rev. X* **8**, 031002 (2018).
- [39] M. Hirschberger, S. Kushwaha, Z. J. Wang, Q. Gibson, S. H. Liang, C. A. Belvin, B. A. Bernevig, R. J. Cava, and N. P. Ong, *Nat. Mater.* **15**, 1161 (2016).
- [40] T. Suzuki, R. Chisnell, A. Devarakonda, Y. T. Liu, W. Feng, D. Xiao, J. W. Lynn, and J. G. Checkelsky, *Nat. Phys.* **12**, 1119 (2016).
- [41] S. C. Huan, D. H. Wang, H. Su, H. Y. Wang, X. Wang, N. Yu, Z. Q. Zou, H. J. Zhang, and Y. F. Guo, *Appl. Phys. Lett.* **118**, 192105 (2021).
- [42] S. C. Huan, S. H. Zhang, Z. C. Jiang, H. Su, H. Y. Wang, X. Zhang, Y. C. Yang, Z. T. Liu, X. Wang, N. Yu, Z. Q. Zou, D. W. Shen, J. P. Liu, and Y. F. Guo, *Phys. Rev. Lett.* **126**, 246601 (2021).
- [43] J. Ge, Y. Z. Liu, J. H. Li, H. Li, T. C. Luo, Y. Wu, Y. Xu, and J. Wang, *Natl. Sci. Rev.* **7**, 1280 (2020).
- [44] T. Murakami, Y. Nambu, T. Koretsune, G. Xiangyu, T. Yamamoto, C. M. Brown, and H. Kageyama, *Phys. Rev. B* **100**, 195103 (2019).
- [45] G. Shi, M. J. Zhang, D. Y. Yan, H. L. Feng, M. Yang, Y. G. Shi, and Y. Q. Li, *Chin. Phys. Lett.* **37**, 047301 (2020).
- [46] L. Q. Zhou, Z. Y. Tan, D. Y. Yan, Z. Fang, Y. G. Shi, and H. M. Weng, *Phys. Rev. B* **102**, 085114 (2020).
- [47] W. B. Ge, P. M. Sass, J. Q. Yan, S. H. Lee, Z. Q. Mao, and W. D. Wu, *Phys. Rev. B* **103**, 134403 (2021).
- [48] Y. H. Liu, L. L. Wang, Q. Zheng, Z. L. Huang, X. P. Wang, M. F. Chi, Y. Wu, B. C. Chakoumakos, M. A. McGuire, B. C. Sales, W. D. Wu, and J. Q. Yan, *Phys. Rev. X* **11**, 021033 (2021).
- [49] S. Wimmer, J. Sánchez-Barriga, P. Küppers, A. Ney, E. Schierle, F. Freyse, O. Caha, J. Michalička, M. Liebmann, D. Primetzhofer, M. Hoffman, A. Ernst, M. M. Otrokov, G. Bihlmayer, E. Weschke, B. Lake, E. V. Chulkov, M. Morgenstern, G. Bauer, G. Springholz *et al.*, *Adv. Mater.* **33**, 2102935 (2021).
- [50] Z. Fisk, D. C. Johnston, B. Cornut, S. von Molnar, S. Oseroff, and R. Calvo, *J. Appl. Phys.* **50**, 1911 (1979).
- [51] P. E. Blöchl, *Phys. Rev. B* **50**, 17953 (1994).
- [52] J. Lehtomäki, I. Makkonen, M. A. Caro, A. Harju, and O. J. Lopez-Acevedo, *Chem. Phys.* **141**, 234102 (2014).
- [53] J. P. Perdew, K. Burke, and M. Ernzerhof, *Phys. Rev. Lett.* **77**, 3865 (1996).
- [54] J. P. Perdew and Y. Wang, *Phys. Rev. B* **45**, 13244 (1992).
- [55] G. Kresse and J. Hafner, *Phys. Rev. B* **47**, 558 (1993).
- [56] G. Kresse and J. Furthmüller, *Comput. Mater. Sci.* **6**, 15 (1996).
- [57] G. Kresse and J. Furthmüller, *Phys. Rev. B* **54**, 11169 (1996).
- [58] E. Liu, Y. Sun, N. Kumar, L. Muechler, A. Sun, L. Jiao, S.-Y. Yang, D. Liu, A. Liang, Q. N. Xu, J. Kroder, V. Stüb, H. Borrmann, C. Shekhar, Z. S. Wang, C. Y. Xi, W. H. Wang, W. Schnelle, S. Wirth, Y. L. Chen *et al.*, *Nat. Phys.* **14**, 1125 (2018).
- [59] B. Meng, H. Wu, Y. Qiu, C. Wang, Y. Liu, Z. Xia, S. Yuan, H. Chang, and Z. Tian, *APL Mater.* **7**, 051110 (2019).
- [60] D. Chen, C. Le, C. Fu, H. Lin, W. Schnelle, Y. Sun, and C. Felser, *Phys. Rev. B* **103**, 144410 (2021).

- [61] J. L. Shen, Q. Q. Zeng, S. Zhang, H. S. Sun, Q. S. Yao, X. K. Xi, W. H. Wang, G. H. Wu, B. G. Shen, Q. H. Liu, and E. Liu, *Adv. Funct. Mater.* **30**, 2000830 (2020).
- [62] J. Chen, X. Xu, H. Li, T. Y. Guo, B. Ding, P. Chen, H. W. Zhang, X. K. Xi, and W. H. Wang, *Phys. Rev. B* **103**, 144425 (2021).
- [63] A. B. Pippard, *Magnetoresistance in Metals* (Cambridge University Press, Cambridge, 1989).
- [64] N. Nagaosa, J. Sinova, S. Onoda, A. H. MacDonald, and N. P. Ong, *Rev. Mod. Phys.* **82**, 1539 (2010).
- [65] Y. Tian, L. Ye, and X. F. Jin, *Phys. Rev. Lett.* **103**, 087206 (2009).
- [66] Q. Wang, Y. F. Xu, R. Lou, Z. H. Liu, M. Li, Y. B. Huang, D. W. Shen, H. M. Weng, S. C. Wang, and H. C. Lei, *Nat. Commun* **9**, 3681 (2018).
- [67] W. L. Ma, X. T. Xu, Z. H. Wang, H. B. Zhou, M. Marshall, Z. Qu, W. W. Xie, and S. Jia, *Phys. Rev. B* **103**, 235109 (2021).
- [68] C. G. Zeng, Y. G. Yao, Q. Niu, and H. H. Weitering, *Phys. Rev. Lett.* **96**, 037204 (2006).
- [69] P. Nozières and C. Lewiner, *J. Phys.* **34**, 901 (1973).
- [70] S. Onoda, N. Sugimoto, and N. Nagaosa, *Phys. Rev. Lett.* **97**, 126602 (2006).